Accurate Robotic Posterior Capsule Polishing with Tissue Stabilization

Yu-Hsiu Lee[1], Yu-Ting Lai[1], Matthew J. Gerber[1], Jaime Dodds[2],
Jean-Pierre Hubschman[2], Jacob Rosen[1], and Tsu-Chin Tsao[1]

Abstract—Within cataract surgery, posterior capsule (PC) polishing is a specific procedure that has demonstrated value towards improving surgical outcomes, yet is not commonly performed by surgeons due to the risk of doing so. In this work, a robotic system is used to perform the polishing procedure through three main contributions: external stabilization of the eye using a dedicated docking device, regulating intraocular pressure through feedback control, and improving the robot-tracking performance to result in an accurate polishing procedure. To validate the methodology, polishing was performed on four *ex vivo* pig eyes by mimicking the residual lens on the PC with an evenly distributed layer of glue. Fast and accurate polishing results were achieved and complete glue removal was accomplished in all experiments without any PC rupture or other surgical complications.

Index Terms—cataract surgery, optical coherence tomography, medical devices, robot-assisted minimally invasive surgery, learning control

I. INTRODUCTION

Cataracts remain the leading cause of blindness worldwide despite the decrease of affected population [1] due to the advancement of cataract surgeries [2]. Despite the maturity of cataract surgery, it is reported that approximately 50% of patients will develop posterior capsule opacification (PCO), which requires follow-up treatment within three years of surgery [3]. While the exact etiology remains unclear, the proliferation and migration of residual lens epithelial cells onto the posterior capsule (PC) is understood to be a primary cause of PCO [4]. Removing residual cells by manual capsule polishing might reduce post-operative PCO but it remains unproven, possibly because it is difficult to ensure complete removal unless meticulous bimanual techniques with specially designed currettes are used [5]. This motivates us to investigate image-guided robotic PC polishing for complete removal of residual cells. If PC polishing can be performed without iatrogenic damage and without increasing post-operative surgical complications, the incidence rate of PCO can be reduced, leading to improved surgical outcomes.

PC polishing involves using an irrigation/aspiration (I/A) handpiece in close proximity to the PC and under low aspiration forces to clean, or "polish," the PC (Fig. 1). Because the
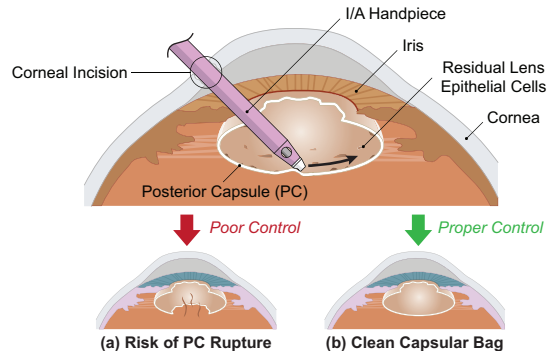
Fig. 1. Top: Illustration of PC polishing with two possible surgical outcomes: (a) Increased risk of PCR due to poor control of the I/A handpiece or aspiration forces and (b) clean capsular bag with a decreased risk of PCO.

PC is a thin (4–9 μm) [6], transparent membrane, the aspiration forces and the position of the I/A handpiece must be well controlled to decrease the risk of posterior capsule rupture (PCR). Due to limited depth sensing, an inability to directly visualize the PC, and poor sensory feedback of aspiration forces, it is not clear that PC polishing done by human is beneficial. Hence, many surgeons choose to skip PC polishing to avoid increasing the risk of PCR [7], [8]. However, accurate tool positioning and enhanced depth sensing can be achieved with a computer-aided robotic system, as our group has previously demonstrated with the Intraocular Robotic Interventional Surgical System (IRISS) [9], [10], [11]. Despite the promise of using a robotic system to perform PC polishing, only one work has addressed this application, which we discuss next.

In our previous work, optical coherence tomography (OCT) was integrated into the IRISS to perform PC polishing [12]. Nine cross-sectional plane scans, i.e. B-scans, were pre-operatively acquired through the center of the pupil and manually segmented to identify the PC shape and location. The segmented pixels were used to reconstruct the PC anatomical structure and generate a PC-polishing trajectory with scheduled aspiration forces. However, this work suffered from at least three significant deficiencies. First, even with the peripheral flesh of the eyeball secured with pins to a designated holder, the interaction force between the I/A handpiece and the corneal incision resulted in eye motion. In addition, the irrigation and aspiration forces of the I/A handpiece resulted in turbulent flows and pressure changes in the intraocular workspace. Together, these conditions cause changes in the structure of the eye which invalidate the pre-operatively generated trajectory. Second, the aspiration forces were pre-operatively scheduled into the trajectory and therefore could

not react to variations in intraocular pressure (IOP) in real-time, causing motion of the intraocular anatomy that were not accounted for. If the procedure were performed in a human patient, this inability to regulate IOP within safe levels could potentially increase the risk of post-operative glaucoma. Third, from a technical standpoint, the dynamic tracking performance of the robot-controlled I/A handpiece was limited by the heuristically determined PID controller, thereby decreasing the tool-tip speed and positional accuracy of the I/A handpiece which might not meet the surgical requirements on a delicate tissue. In this paper, we address these three issues through (a) physically constraining the eye, (b) regularizing IOP, and (c) improving robot-tracking performance.

First, commercially available eye-docking devices such as those used in femtosecond-laser assisted cataract surgery (FLACS) have shown effectiveness in stabilizing the eye sufficiently well to perform corneal incision, capsulorhexis, and lens fragmentation with a femtosecond laser [13]. However, use of these devices prohibits the simultaneous use of intraocular tools: when the docking device is engaged, no surgical instruments can enter the eye. While this reality is not an issue in FLACS (where a laser does the work), it is a prohibitive constraint in robot-assisted intraocular operations that use physical tools.

Second, although some work has addressed controlling IOP [14], [15], only the function was demonstrated and there was no analysis of the underlying physics of the eye. Furthermore, IOP control was done in a two-hour period [15], which does not have the bandwidth to drastic IOP changes during intraocular operations. The measurement of IOP has also been discussed in other work [16], [17], but the demonstrated devices were purely for data acquisition and were not integrated into a system for IOP regulation.

Third, in light of numerous existing studies on precise tracking control, we aim at a computationally-efficient method that can increase the joint bandwidth and is practically implementable on the IRISS. Therefore, a data-driven feedforward controller from iterative learning of inverse joint dynamics was adopted to further improve the performance of existing servo controllers.

We identified the technical challenges of the delicate PC polishing procedure, and converted the clinical requirements to technical requirements for robotic surgery. Our work is the first to carry out the design, modeling, analysis and an innovative mechatronic system comprising three methods to enable, for the first time, efficient and effective robotic intraocular lens capsule polishing. The system overview and methodology is introduced in Section II, followed by the three main contributions. Section III shows the docking device for eye stabilization, Section IV discusses the IOP modeling and regulation, and Section **??** elaborates the accurate trajectory tracking through the use of feedforward filters. Then, experimental results and technical evaluations are presented in Section VI. Finally, Section VII reviews the outcomes and significance of the proposed methodology.
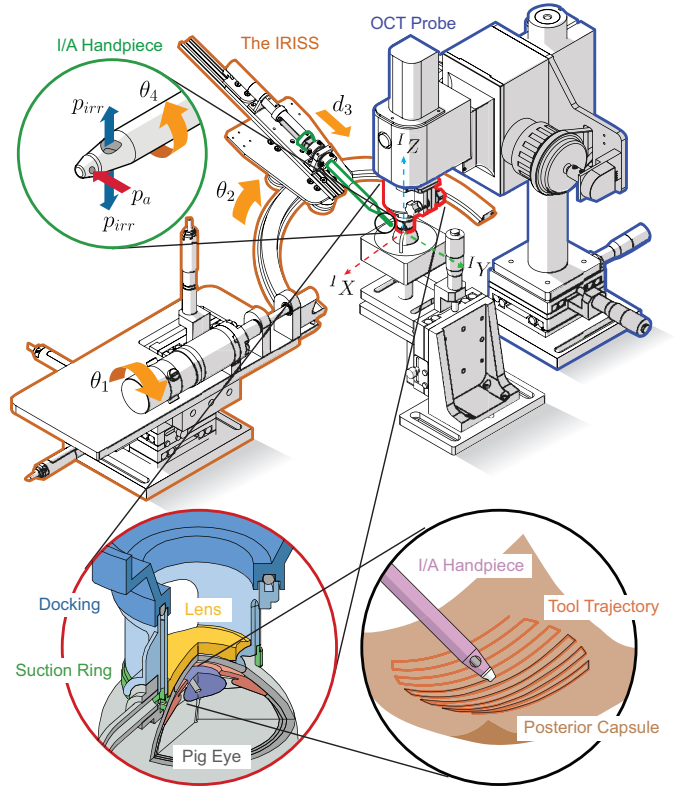

Fig. 2. The system overview.

II. System Overview and Methodology

The enabling technologies for accurate PC polishing are highlighted in Fig. 2. These components include (a) an eye docking device (Section III), (b) intraocular pressure regulation with the I/A headpiece (Section IV), and (c) accurate trajectory tracking control of the instrument tip (Section **??**). For a detailed description of the mechanism design and mechatronic architecture of the robotic platform IRISS, readers are referred to the work in [9], [10], [12].

The flowchart of the proposed methodology for robot-assisted PC polishing is illustrated in Fig. 3, indicating the role and involvement of each component throughout the procedure. First, balanced salt solution (BSS) is applied to the eye and the docking device is engaged. The BSS provides hydration to the cornea and the docking suppresses involuntary eye movement. Then, the instrument tip is partially inserted to enable irrigation and make the pre-operative environment as close as possible to the intra-operative condition while maximizing the field of view of OCT to reconstruct pre-operative eye anatomy. Once inserted, the IOP regulation is engaged to account for the pressure drop due to leakage from the corneal incision. When the pressure is stabilized, the OCT is commanded to acquire a three-dimensional volume scan of the anterior chamber, and a polishing trajectory tailored for the scanned anatomy is generated. Based on the trajectory, the tracking control algorithm is applied to command the polishing motion with improved accuracy. During the tool motion, the docking mitigates eye motion due to the surgical force applied at the corneal incision; the IOP regulation ensures the integrity

TABLE I
ABBREVIATIONS AND DEFINITIONS USED IN THIS PAPER.

Abbreviation	Definition	Explanation
IRISS	Intraocular Robotic Interventional Surgical System	The robotic system used in this work
PC	Posterior Capsule	The thin, transparent membrane at the back of the eye lens
PCO	Posterior Capsule Opacification	Clouding of the PC following cataract surgery
PCR	Posterior Capsule Rupture	Breakage of the PC—a serious surgical complication
IOP	Intraocular Pressure	Pressure inside the anterior chamber
ILC	Iterative Learning Control	A learning scheme that uses prior trial to improve subsequent trials.
OCT	Optical Coherence Tomography	A noninvasive imaging modality utilizing low-coherence interferometry.
RCM	Remote Center of Motion	A mechanically fixed point about which the IRISS is constrained to move.

of the anatomical structure while preventing the tool from damaging the PC with excessive aspiration force. After the completion of the trajectory following, the tool halts at the periphery of the OCT view and a verification OCT scan is performed to assess the surgical outcome. If the result is satisfactory, the IOP control disabled, the I/A handpiece is retracted, and the docking is disengaged.

III. EYE STABILIZATION –DOCKING DEVICE

For image-guided eye surgery, it is of desire to fixate the eye globe. Fixation of the globe not only results in better imagery, but also improves the safety and surgical outcomes. In FLACS, the eye is stabilized by an external docking device, such as LenSx SoftFit (Alcon, Texas, USA) and Visumax (Carl Zeiss, Germany). The docking device suctions onto the eye and enables high-quality OCT imaging for planning the trajectory of the laser, and serves to maintain the steadiness of the globe during the laser-assisted operations. These features are desirable for cataract surgery as well, as the surgical tool may displace the eye globe via friction and physical interference, thereby invalidating preoperatively obtained data of intraocular anatomy and planned trajectories. However, existing docking device cannot be directly applied since it interferes with the workspace of the surgical tool. To address this issue, we have developed a custom docking device that maintains eye stability through external suction while enabling surgical access to the intraocular workspace (Fig. 4)

The design requirements for the docking device were:

1) Unobstructed optical path from the transpupillary imaging device to the eye
2) Stabilize eye motion to within 100 μm of displacement during intraocular procedures
3) Maintain corneal hydration for the duration of a surgical procedure
4) Enable access to the intraocular workspace for two surgical instruments
5) Conform to the curvature of the cornea

The disposable device can be easily connected to and detached from the transpupillary OCT system. A customized lens with two cutouts provides physical space for a pair of surgical instruments to pass through a pair of corneal incisions and allows for bi-manual operations. The clear acrylic lens has a constant 2 mm thickness to prevent image warping from different lengths of optical paths. Underneath is a deformable suction pad that provides sealing and restrains the eye motion. The body was fabricated from ABS via 3D printing and the suction ring overmolded from a rubber-like photopolymer (Agilus 70A, Stratasys).

Fig. 5 presents the tool range of motion when the docking is applied. The 120° azimuth angle and up to 50° elevation angle are based on the studies in [18] for anterior segment surgery. The fabricated device will be evaluated in Section VI-A.

IV. CONTROL-ORIENTED MODELING FOR INTRAOCULAR PRESSURE REGULATION

During PC polishing, the IOP varies due to the I/A forces within the anterior chamber, the mechanical stress applied on the cornea by the I/A handpiece, and the aqueous flow out of the anterior chamber [19]. When IOP is lower than the nominal 12–22 mmHg range [20], the cornea can suffer structural collapse, which has the side effect of severely distorting acquired OCT data. In addition, low IOP also causes the PC to "come up" towards the pupillary plane, dramatically increasing the risk of PCR. For these reasons, IOP regulation during PC polishing could increase the safety of PC polishing.

1) Hydro-Mechanical Model: To facilitate the control design for IOP regulation, the open-loop model is shown in Fig. 7a, wherein the actuator dynamics, the tool fluid path, and the anterior segment are described with different colors. The anterior segment is modeled as a one degree of freedom hydromechanical system. This open-loop model will later be utilized for the feedback control design. Three main fluid paths are included: (1) Q_{irr}, inflow due to the higher pressure p_{irr} at the irrigation port of the I/A handpiece, (2) Q_{asp}, outflow due to the lower pressure p_{asp} at the aspiration port of the I/A handpiece, and (3) Q_{leak}, leakage out of the anterior chamber to atmospheric pressure p_{atm} through the corneal incision. The stiffness of the cornea, K_{ant}, and the effective stiffness of the PC, K_{post}, also affect IOP. In this model, the IOP, p_{iop}, can be determined from the interaction of the eye mechanics and the fluid dynamics of the I/A handpiece. Specifically, the resistive elements R_{leak}, R_{irr}, and R_{asp} determine the pressure differences:

$$R_{leak}Q_{leak} = p_{iop} - p_{atm} \qquad (1)$$
$$R_{irr}Q_{irr} = p_{irr} - p_{iop} \qquad (2)$$
$$R_{asp}Q_{asp} = p_{iop} - p_{asp} \qquad (3)$$

The flow resistance values can be computed from the known geometry of the coaxial-type I/A handpiece (8172 UltraFlow; Alcon Laboratories, Inc.) used [21].

Assuming the fluid is incompressible, then from continuity:

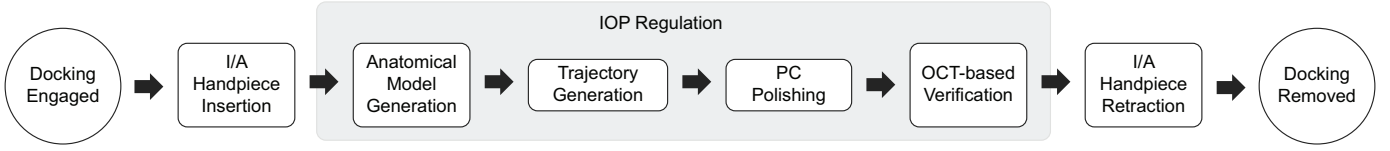$$\sum_i Q_i = A_{ant}\dot{x}_{ant} + A_{post}\dot{x}_{post}, \qquad (4)$$

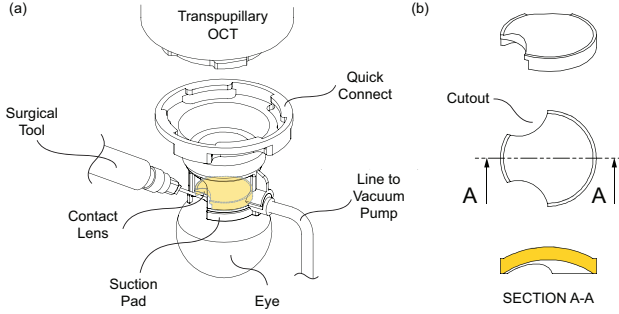Fig. 3. Flowchart of the PC-polishing process.

Fig. 4. Docking apparatus for eye stabilization. (a) Isometric view of the docking, which is connected to transpupillary OCT. (b) Customized lens with cutout for tool access.
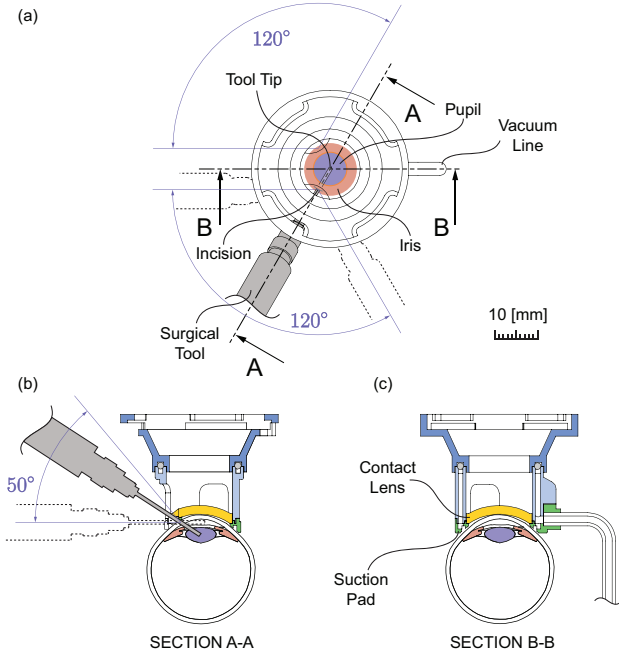

Fig. 5. (a) Top view of the docking, which supports access of two tools with $120°$ range of motion. (b) Sectioned view along plane A-A, showing the maximum elevation angle up to $50°$. (c) Sectioned view along plane B-B, showing the passage for vacuum suction.

where A_{ant} is the effective area of the corneal surface, $\dot{x}_{ant}$ is the displacement velocity of the corneal surface, A_{post} is the area of the PC, and $\dot{x}_{post}$ is the displacement velocity of the PC (Fig. 6). Balancing forces gives rise to:

$$K_{ant}\left(x_{ant} - x_{ant}^0\right) = A_{ant}\left(p_{iop} - p_{atm}\right) \qquad (5)$$

$$K_{post}\left(x_{post} - x_{post}^0\right) = A_{post}\left(p_{iop} - p_{vit}\right) \qquad (6)$$

where p_{vit} is the pressure in the posterior chamber exerting upward onto the PC surface and $x_{(\cdot)}^0$ are the undeformed
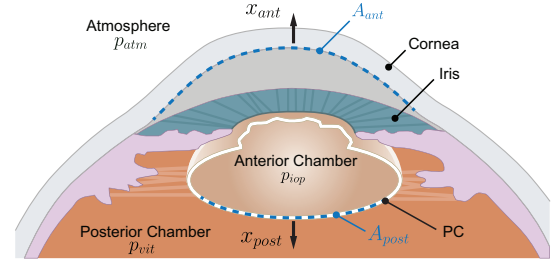

Fig. 6. Illustration of anatomical structures and important physical variables.

positions. The stiffness values are determined by the radial deformation of the cornea and the PC, which are assumed to be thin-walled spherical shells [20].

To summarize, Equations (1)–(6) constitute the lumped dynamical system governing the IOP response. Gauge pressure is used ($p_{atm} = 0$) to simplify the notation, and we assume $\dot{p}_{vit} \approx 0$ because the volumetric ratio between the posterior [22] and anterior chamber [23] results in a 25 times less vitreous pressure change. The resultant system dynamics can be written as the following state-space representation with p_{iop} as the state, p_{asp} as the input, and p_{irr} as a constant forcing term.

$$\underbrace{\dot{p}_{iop}}_{\dot{x}} = \underbrace{\frac{(R_{irr}^{-1} - R_{leak}^{-1} - R_{asp}^{-1})}{(\theta_{ant} + \theta_{post})}}_{A}\underbrace{p_{iop}}_{x} + \underbrace{\frac{R_{asp}^{-1}}{(\theta_{ant} + \theta_{post})}}_{B}\underbrace{p_{asp}}_{u}$$
$$+ \underbrace{\frac{R_{irr}^{-1}}{(\theta_{ant} + \theta_{post})}}_{F}\underbrace{p_{irr}}_{w}$$

$$(7)$$

with $\theta_{ant} = \frac{A_{ant}^2}{K_{ant}}$ and $\theta_{post} = \frac{A_{post}^2}{K_{post}}$. Taking the Laplace transform, we can represent the dynamics as

$$P_{iop} = G_{asp}P_{asp} + G_{irr}P_{irr} \qquad (8)$$

where G_{asp} and G_{irr} are the transmissions $\frac{P_{iop}}{P_{asp}}$ and $\frac{P_{iop}}{P_{irr}}$

$$G_{asp} = -[(\theta_{ant} + \theta_{post})R_{asp}s + (\frac{R_{asp}}{R_{irr}} - \frac{R_{asp}}{R_{leak}} - 1)]^{-1}$$
$$G_{irr} = [(\theta_{ant} + \theta_{post})R_{irr}s + (1 - \frac{R_{irr}}{R_{leak}} - \frac{R_{irr}}{R_{asp}})]^{-1}$$

$$(9)$$

In static transmission ($s = 0$), the term $(\frac{R_{asp}}{R_{irr}} - \frac{R_{asp}}{R_{leak}} - 1)$ in G_{asp} is greater than 0, therefore increasing the aspiration force will result in a decrease in IOP. Similarly, $(1 - \frac{R_{irr}}{R_{leak}} - \frac{R_{irr}}{R_{asp}})$ in G_{irr} is also greater than 0, hence positive irrigation will increase IOP.

2) Actuator Dynamics and Open-Loop Response: To validate the open-loop model from p_{asp} to p_{iop}, different step vacuum commands were applied on the Alcon Accurus surgical system (Model 800CS; Alcon Laboratories, Inc.) with the maximum controllable aspiration pressure of 600 mmHg, and $p_{irr} = 60$ mmHg was set up by the gravity feed of the water bottle filled with BSS. In each experiment, p_{asp} and p_{iop} were measured using an inline pressure sensor (24PCCFG6G, Honeywell International Inc., Charlotte, NC, USA) and a PCB-mounted pressure sensor (ABPDANT015PGAAS, Honeywell International Inc., Charlotte, NC, USA).

Aside from the passive elements of the hydro-dynamical model in Section IV, the dynamics from vacuum command p_{asp}^* to actual p_{asp} in Fig. 7 are also identified. The identification of the Accurus machine was done using a step input of 100 mmHg step size as the vacuum command and the resultant normalized step response is shown in Fig. 8 with the data sampling rate of 100 Hz. A transmission delay of 0.11 seconds was observed in the actuator dynamics. To construct an open-loop model, the unit pulse response was first constructed using one-step shift and subtraction from the step response data. After the delay is accounted for, a 10-th order discrete-time state-space and a reduced 4-th order state-space models were realized using the Ho-Kalman method, and are compared to the experimental data as in Fig. 8.

With a complete open-loop model from p_{asp} to p_{iop} with nominal system parameters and identified actuator dynamics from p_{asp}^* to p_{asp}, open-loop responses between simulation and experiment are compared in Fig. 9. Step vacuum commands (p_{asp}^*) were applied at $t = 0$ (sec) on the I/A handpiece and resulting IOP was recorded. Though they have the same order of magnitude and similar exponential growth trends, it is observed that the change in IOP deviates by approximately 20 %, whereas the rise time is 0.08 s for the simulation and 0.2 s for the experiment. The discrepancy of time constants is attributed to the parameter values assigned to the model as every eye is different. Slow drifts are also present in the experimental data. Therefore, pressure regulation requires feedback control (Fig. 7b).

V. TRAJECTORY TRACKING CONTROL

The PC polishing requires the instrument tip to slightly touch the PC while moving laterally to scan the surface. With the eye externally stabilized by the docking device (Section III) and the lens internally stabilized by the IOP regulation (Section IV), the intraocular surgical workspace is maintained stationary within 100 μm. Therefore, we can treat the PC polishing as a trajectory tracking problem, where the objective is to accurately follow a prescribed instrument tip trajectory. This is achieved by the robot's multi-axis coordinated joint motion control via the inverse kinematics from the task to joint space. For precise trajectory tracking, feedforward actions are required to compensate for inevitable dynamic delays of the servo feedback control. Iterative learning control (ILC), which learns the feedforward compensations for a desired trajectory and adds them to the servo feedback control, has been well established. However, it is impractical to perform the ILC
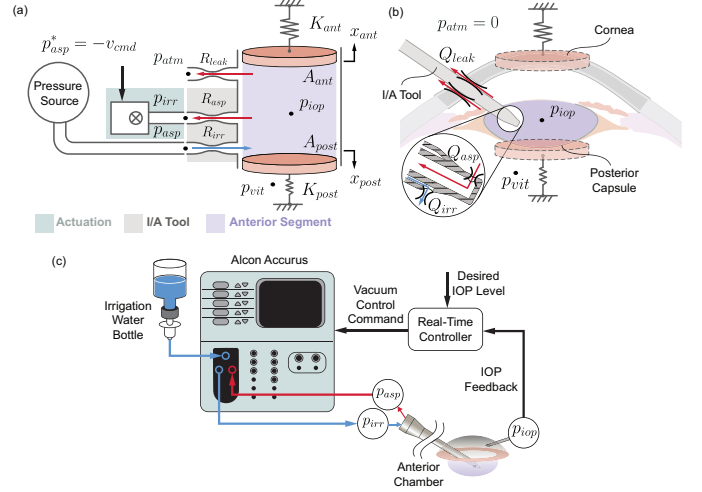

Fig. 7. Open-loop modeling and control of intraocular pressure. (a) Modeling elements in the anterior chamber. (b) The hydro-mechanical sub-system of the anterior segment. (c) The simplified hydro-mechanical model.
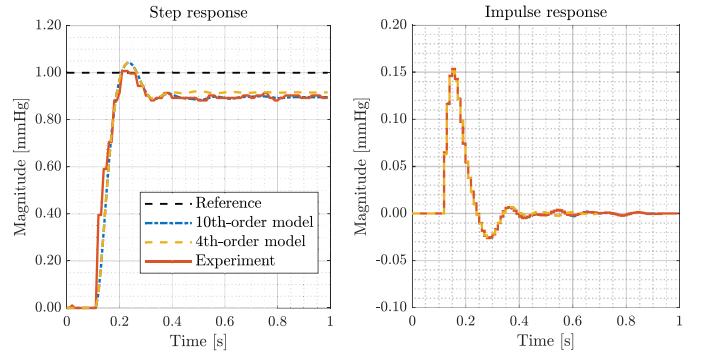

Fig. 8. Actuator dynamics of the Accurus machine. The normalized step response is obtained by commanding a 100 mmHg step size vacuum command v_{cmd}.
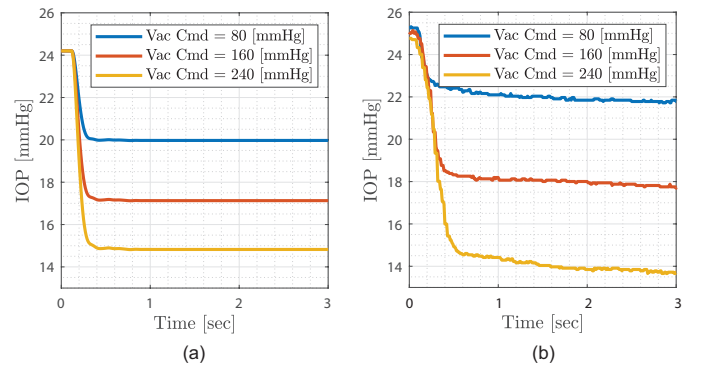

Fig. 9. Open-loop IOP responses under different vacuum command levels from (a) simulation model and (b) experiment with an *ex vivo* pig eye.

process in every surgery to learn the feedforward control for the specific desired trajectory of the PC surface created in situ by the OCT scans. Hence, we created feedforward filters and applied them in situ to any desired trajectories. The feedforward filters do not alter the existing servo controllers and normally require less data memory than the ILC feedforward trajectories.

Due to the orthogonality of the joint axes of the IRISS robot, the dynamics can be decoupled into single-input-single-output systems. The input-output relationship from a position reference command $r(k)$ to the resultant joint motion $y(k)$ sensed by the encoder is represented by a transfer function $G(z)$, where k is the time index and z is the $\mathcal{Z}$-transform variable. Ideally, if the inversion $F(z) = G^{-1}(z)$ exists, it can be used as a feedforward filter and the output y of the cascade system GF follows the input $r(k)$ exactly:

$$y(k) = \underbrace{G(z)F(z)}_{1} r(k) \approx r(k) \qquad (10)$$

Herein the feedforward controller $F(z)$ is generated via a data-driven algorithm which recursively learns the dynamic inversion [24] of the joint axes. Data-driven approach is preferred over model-based design as the former is not susceptible to modeling errors. Furthermore, the specific algorithm in [24] directly constructs a non-parametric finite-impulse-response (FIR) inverse filter $F(z) = \sum_{k=-N/2}^{N/2} f(k)z^{-k}$ which mitigates fitting loss and can achieve precise control for both minimum- and non-minimum-phase systems. As an example, FIR inverse dynamics of joint θ_1 is presented in Fig. 10. The feedforward filters for all joints only need to be learned once before the robot is put into use. For technical details, the readers are referred to the original work in [24].
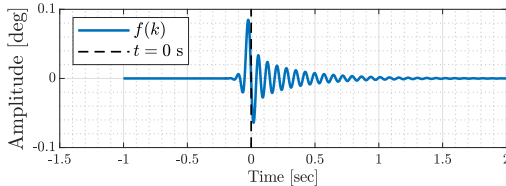

Fig. 10. Non-causal FIR inverse dynamics of the first joint θ_1.

VI. EXPERIMENTAL RESULTS

A. Evaluation of Docking Apparatus

It is known that frequent corneal hydration is critical for maintaining high-quality OCT visualization of the intraocular workspace as well as avoiding corrugation of the corneal surface. To demonstrate that the use of the docking device maintains OCT signal quality, the following experiment was performed.

An *ex vivo* pig eye was prepared by removing the lens and injecting sufficient lubricating jelly into the capsular bag and anterior chamber to maintain its natural structure. The eye was secured within the sensing range of the OCT probe and continuous B-scans were acquired at a rate of 2 Hz through the center of the eye. In the case of no docking, the cornea was hydrated at $t = 0$; in the case of docking, the cornea

hydrated, then the docking was immediately applied at $t = 0$. The short (approximately 5 s) delay due to the docking being applied is unimportant for the following analysis.

To quantify "signal quality," a signal-to-noise ratio (SNR) was defined as

$$\text{SNR} = 10 \cdot \log_{10}\left(\frac{S_s}{S_n}\right) \qquad (11)$$

where

$$S_s = \sqrt{\frac{1}{n_s} \sum_{i,j} I_{i,j}^2}, \quad S_n = \sqrt{\frac{1}{n_n} \sum_{i,j} I_{i,j}^2} \qquad (12)$$

and where n_s is the number of signal pixels, $I_{i,j}$ is the pixel intensity of pixel i,j, and n_n is the number of noise pixels. The signal and noise pixels were identified through manual segmentation of the OCT B-scans by an experienced labeler.

The results show a comparatively fast decrease in SNR in the case of no docking compared to the case with docking, which decreases more slowly (left side of Figure 11). From the OCT B-scans, it can clearly be seen that the signal strength of the PC degrades over the trial time in the case of no docking (right side of Figure 11), further implying that the docking maintains corneal hydration.

To verify intraocular tissue stabilization of the docking, tissue motion was compared with and without docking subject to robot motion. A parabolic trajectory was designed at the iris plane with a travel distance 2 mm. Intra-operative B-scans were recorded during robot motion and the mean intensity was used as the threshold to binarize each image. Once the high-intensity region was identified, cornea and iris were segmented based on prior knowledge of the location in the image. Then the centroid of each tissue was determined by finding the mean value of the segmented region.

The displacement of the tissue due to tool motion was compared with the previous time frame. Hence, the Euclidean distance was calculated as the norm of the current tissue centroid with respect to the previous tissue centroid. Fig. 12(a) shows an example of tissue motion comparison between $t = 0$ and $t = 6$ s without docking. This serves as a baseline for comparison to the tissue motion when the docking was applied (Fig. 12b). We evaluated the pixel correlation (R^2 value) on the B-scans to identify the tissue motion between the tool locations at different time. This was computed as:

$$R = \frac{\sum_m \sum_n (I_{0,mn} - \bar{I}_0)(I_{6,mn} - \bar{I}_6)}{[\sum_m \sum_n (I_{0,mn} - \bar{I}_0)^2 \sum_m \sum_n (I_{6,mn} - \bar{I}_6)^2)]^{1/2}} \qquad (13)$$

where I_0 is the B-scan image at $t = 0$, I_6 is the B-scan image at $t = 6$ s. $\bar{I}_0$ and $\bar{I}_6$ represents the mean of that image.

The correlation (R^2) values of each tissue were also computed as a metric to evaluate the effectiveness of the docking. Larger R^2 value means there is greater correlation between the two images and therefore less tissue movement in terms of pixel movement. The R^2 value for cornea increases from 0.69 without the docking to 0.98 with the docking, while the R^2 value for the iris increases from 0.64 to 0.89.

Tissue movement over the course of the tool trajectory was computed using the same Euclidean distance calculation
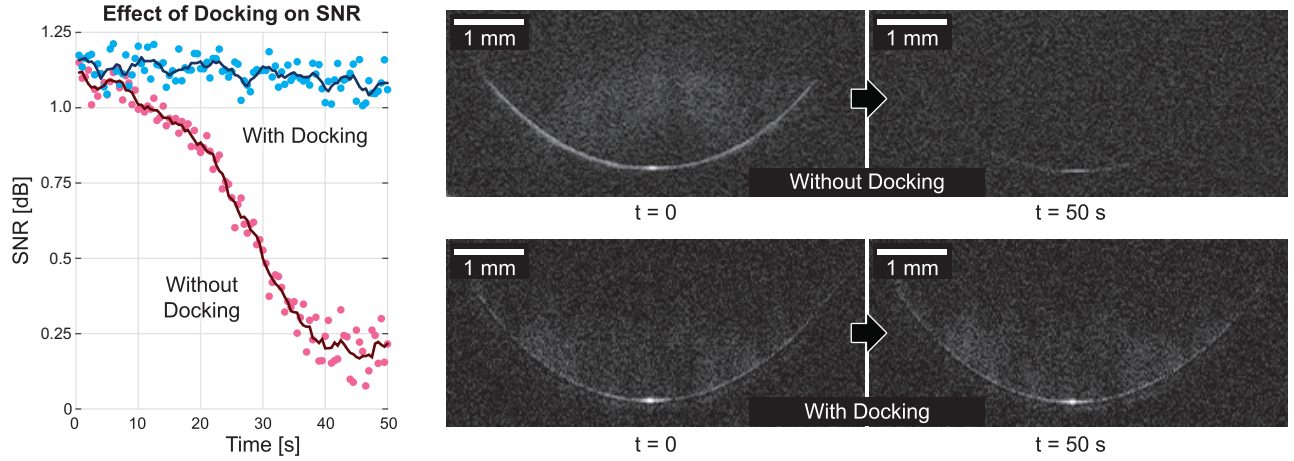
Fig. 11. Left: The effect of docking on signal-to-noise ratio (SNR) over time; red and blue points are values of SNR calculated from Equation 11 and the trend lines are five-point centered moving averages intended to aid in visualizing the trends. Right: OCT B-scans with and without docking acquired immediately at trial start ($t = 0$) and at trial end ($t = 50$ s), showing a clear decrease in signal strength in the case of no docking.
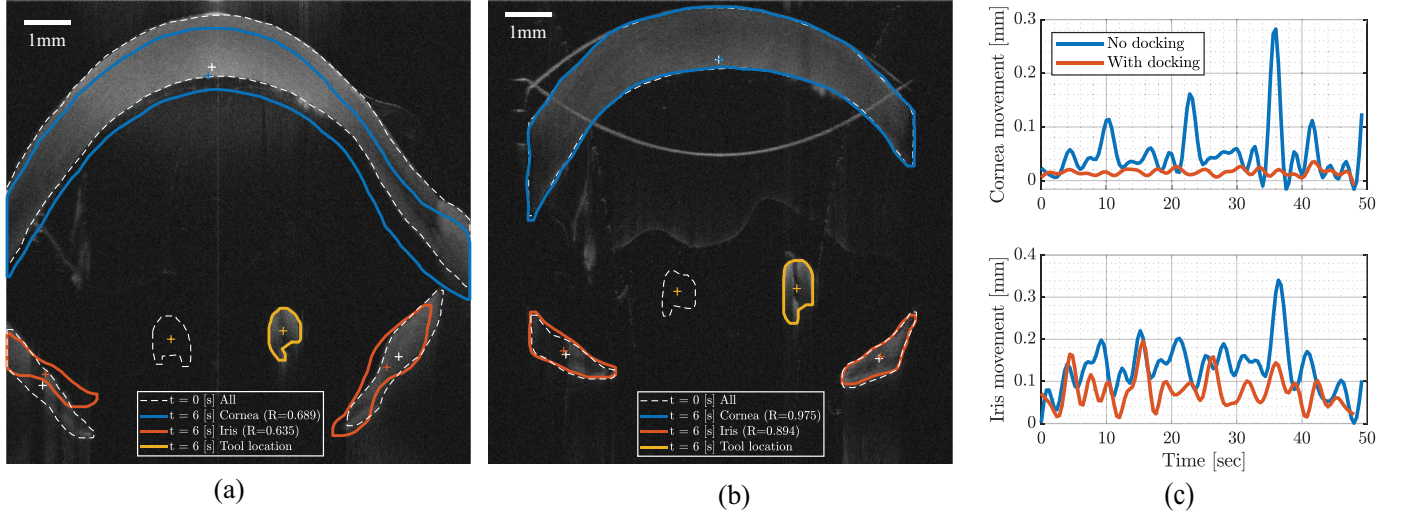

Fig. 12. Intraocular tissue motion with and without docking. (a): Pig eye without docking. (b): With docking. White-dotted lines indicates initial locations of each tissue at $t = 0$s. The tissue motions are shown in colored solid lines at $t = 6$s. The tool is shown in the middle and was commanded to move a parabolic trajectory with a travel distance of 2 mm inside the eye.

(Fig. 12c). The docking reduces the RMS error of the cornea movement by 76% because the docking lens is directly applied to the cornea surface to create stabilization. However, it only decreases 33% on the RMS error of iris movement because docking provides external stabilization and therefore intraocular environment is not entirely constrained by its presence or use.

B. Closed-Loop Controller and Optimization for Intraocular Pressure Control

A model-based proportional-integral (PI) controller was designed to regulate the IOP and avoid structural collapse of the anterior chamber. The controller parameters were tuned based on the constructed hydro-mechanical model with a sampling rate of 100 Hz. To account for model differences between each eye, the resultant controller was ensured to have sufficiently large gain and phase margins for robustness.

The parameters of the controller went through optimization techniques to minimize the steady-state error with respect to a step response, e. The integral time absolute error $J = \sum_k k|e(k)|$ was used as the cost function with proportional and integral gains as the optimizer, where the $|\cdot|$ is the absolute operator. The optimization was initialized by the standard Ziegler–Nichols method and the gradient-descent method was used to minimize the cost function. The resultant PI controller was as follows:

$$C_{PI}(z) = 1.25 + \frac{0.25}{z - 1} \quad (14)$$

with a 5.97 dB gain margin and an 119.2° phase margin.

To verify the controller design, the step response from simulation was compared with the experimental results (Fig. 13). The initial IOP levels were set such that both were under the same initial condition. The full-order model explains the general behavior of the closed-loop system responses, including the higher-order actuation dynamics after the loop

was closed, whereas the reduced-order model does not capture the transient dynamics. This results in a settling time of 4 s and an additional 2 s in rise time.
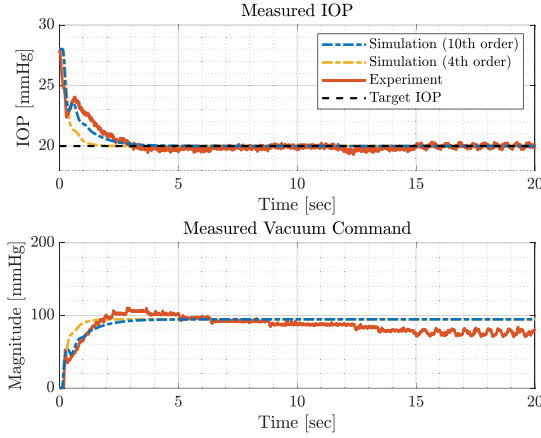

Fig. 13. Closed-loop IOP step responses with optimized parameters.

C. Motion Tracking Performance

To clean up the entire visible PC and ensure the completeness of PC polishing, three types of trajectory were compared and analyzed (Fig. 14). Intuitively, raster scan trajectory was created to cover the visible PC with the velocity profile scheduled to zero at turning corners and maximum speed otherwise. However, the acceleration profile was large and contained pulses due to aggressive changes in the velocity. Hence, the sinusoidal scan was developed to resolve the aggressive acceleration, as well as rounding sharp corners in the raster scan trajectory. A Lissajous curve also holds the property of smooth velocity and acceleration without sharp corners.

Feedforward filter design for each joint was independently conducted due to different bandwidths of the motors. The bandwidth of the reference models were specified to push the tracking performance without saturating the actuators. An integrator was used for $H(z)$ for every joint with a step size of $1°$, then $H(z)\delta_M(k)$ was assigned as the reference signal for the system. To design a good compromise between robustness and performance of the FF learning, Q-filtering was added to each joint: 6 Hz for joint 1, 2 Hz for joint 2, and 12 Hz for joint 3.

To demonstrate the converged FF control, the robot was commanded to track the above three trajectories in three dimensions with the learned FF filters applied on each joint. The dynamic tracking error was mitigated by means of joint dynamic inversions (Table II). Due to the fastest tracking time and superior performance, the sinusoidal scan is chosen for the following *ex-vivo* PC polishing experiments. The time history errors for tracking the sinusoidal pattern shown in Fig. 15 demonstrate the significant improvement with the feedforward filters.

D. Ex-Vivo Pig Eye Experiments

1) Setup and Alignment: Ex vivo pig eyes (Sioux-Preme Packing) were used as the eye model for the PC polishing
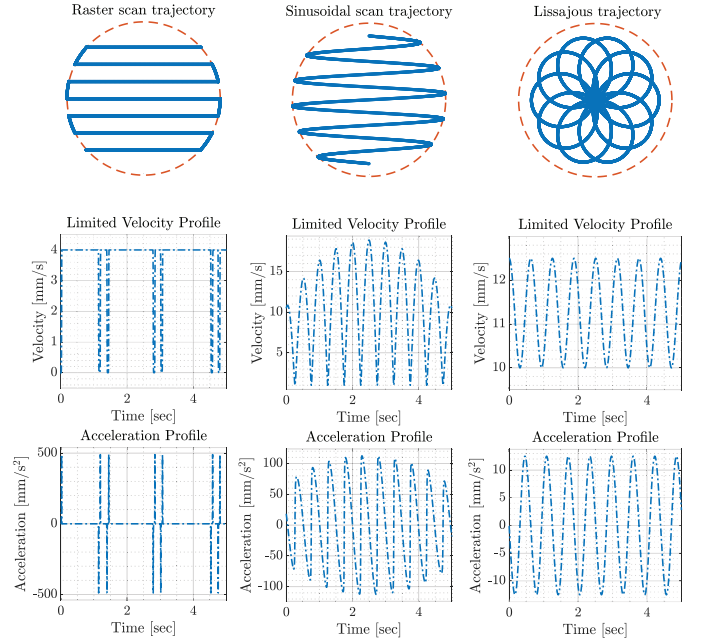

Fig. 14. Trajectories used in robot motion tracking with the FF filtering. Top row: trajectories viewing from the top. Second row: velocity profile for each trajectory. Bottom row: acceleration profile for each trajectory.
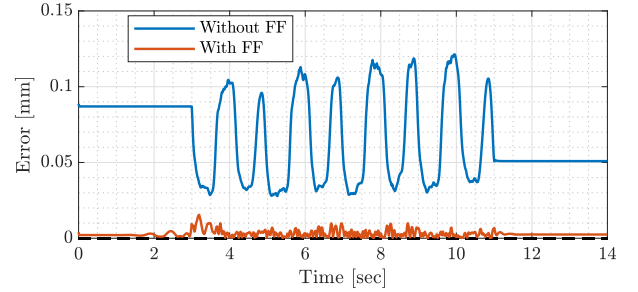

Fig. 15. The time history of the tracking error of the sinusoidal scan trajectory.

TABLE II
RMS ERROR WITH AND WITHOUT FF FILTERS FOR EACH TRAJECTORY.

	without FF (μm)	with FF (μm)	Percent Decrease (%)	Time (s)
Raster Scan	49.4	7.9	83.9	30
Sinusoidal Scan	71.6	3.6	94.9	12
Lissajous Curve	92.9	7.1	92.4	17

experiments. During the experiment, the unscalded eyes were secured into a custom-made polystyrene holder. Preparation of each eye was performed under a surgical microscope (M840, Leica Microsystems, GmbH). A 3.0 mm keratome blade was used to create a bi-planar incision, followed by a 8–9 mm diameter continuous curvilinear capsulorhexis. Hydrodissection and hydrodelineation were done using BSS (NDC 0065-0800-50; Alcon). After manually removing the emulsified lens material, approximately 0.01 ml of water-soluble glue was injected onto the PC, using a 21–Ga blunt–tip cannula. The glue represented residual lens epithelial cells adhered to the PC to be cleaned by the robotic system. The volume introduced was chosen by initial experiment which ensures the glue sufficiently covered the PC with appropriate thickness. Finally,
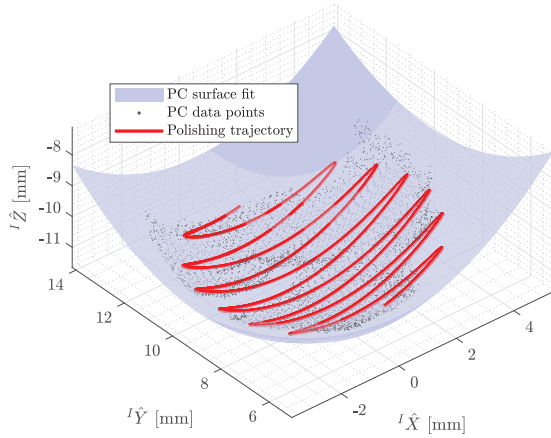
Fig. 16. Trajectory generation based on a volume scan of the OCT. The black dots represent actual point cloud. The blue surface is the surface fit of the point cloud. The red line indicates the trajectory generation.
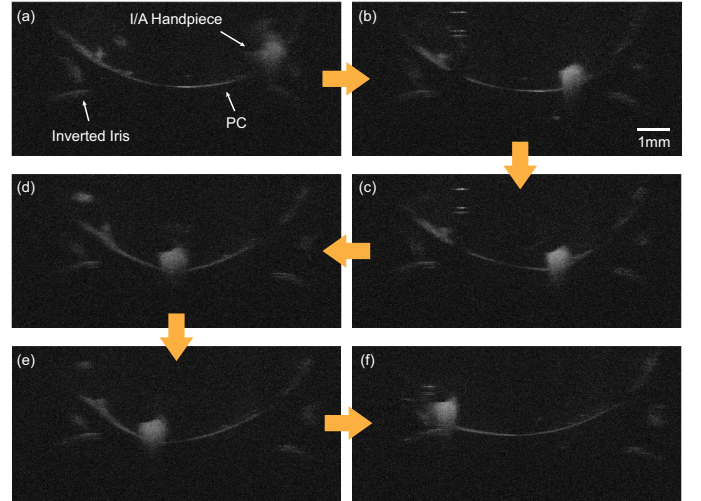

Fig. 17. Per-opretative B-scan images (a to f sequentially) acquired at 10 Hz and visualized during PC polishing experiment. The PC is being pushed down by the I/A handpiece tooltip and the OCT scans at the tooltip during PC polishing.

a sterile lubricating jelly (MDS032290H, Medline) was proven to be similar to ophthalmic viscoelastic gel and was used to fill the anterior chamber to prevent structural collapse and maintain the shape of the capsular bag.

2) Planning: Following eye preparation, the docking was applied and the I/A handpiece commanded such that the tip was approximately 2 mm inside eye through the corneal incision with the irrigation at 65 mmHg. This introduces irrigation into the anterior chamber, filling the capsular bag and pushing the PC downwards into its natural shape and location. At this point, the IOP control was engaged and a volume scan was acquired of the posterior capsule. The IOP control ensures the subsequent model would be consistent with the later polishing environment.

The acquired volume scan data was loaded into memory, scaled to a pixel intensity range of $[0, 1]$, and then converted to binary with a heuristically chosen threshold of 0.6. The largest (by number of pixels) 3D binary blob was retained and these points converted to Euclidean coordinates using the known pixel-to-millimeter ratio provided by the OCT manufacturer and then converted to the IRISS coordinate frame using the known coordinate transformation [12].

The most-posterior data point in each A-scan was identified and used to fit a second-order polynomial surface to this data and displayed to the operator via a custom GUI. In all trials, this initial surface fit was not assumed to be accurate and was provided to the operator as an initial guess which can then be tweaked in terms of position, orientation, and surface-fit parameters. The visualization of the polynomial fit was then displayed with the fitting residuals. Once satisfied, the operator could choose to proceed with the trajectory generation and subsequent execution of PC polishing.

The trajectory was first generated in the XY two-dimensional space and was parameterized by radius, travel distance, number of repetitions, and maximum tool-tip velocity. The radius determined the area to be cleaned up during PC polishing and was adjusted based on the visible PC data points. The travel distance indicated that the horizontal travel length in the direction of $^I Y$ (Fig. 2). The points were then

vertically projected onto the polynomial surface of the PC fit to determine the depth information, which makes the overall trajectory three-dimensional (Fig. 16). Note the dimension of the I/A handpiece tip ($r = 500$ µm) was taken into account in the trajectory planning such that the instrument was always in contact with the PC surface (Fig. 17). Finally, the target IOP was set for each trial according to the eye condition and the range of nominal IOP [20].

TABLE III
TABULATED RESULTS OF PC POLISHING.

Trial No.	1	2	3	4
PC polishing time (s)	12	36	20	25
Percent removal (%)	98.7	99.6	99.2	99.1
No. of cycles	1	2.5	1.5	2
Distance travelled (mm)	66.92	167.33	100.4	133.86
PC rupture	No	No	No	No

3) Evaluation of Posterior Capsule Polishing: The PC polishing experiment was conducted on four *ex vivo* pig eyes (Table III). The evaluation metrics focused on four factors: polishing time, percentage of glue removal, aspiration force, and PC rupture. In general, the OCT acquisition time was consistent (approximately 45 s). The polishing time was calculated based on automatically acquired timestamps of each process and the duration was defined as the time between the start and end of the polishing. This took up 12–36 s depending on the number of cycles needed.

The effectiveness of the cleaning was evaluated on the glue volume between pre-operative and post-operative volume scans. The scan parameters (volume scan size and reference intensity) were consistent across all trials in order to maintain similar diffusion and optical paths. After volume scan acquisition, a constant scaling factor was applied on each raw intensity data and binarized with a constant threshold value. Manual segmentation on the glue was performed on the entire B-scan stack by an experienced labeler and the pixel labels were transformed to a physical volume. Only
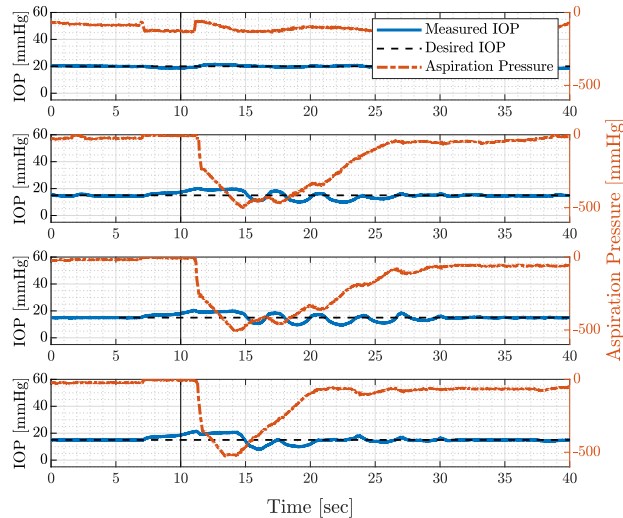
Fig. 18. The pressure during PC polishing of four different *ex vivo* pig eyes. The robot starts polishing procedure at 10 seconds. The blue line is the measured IOP corresponding to the left axis and the red line is the aspiration pressure corresponding to the right axis.
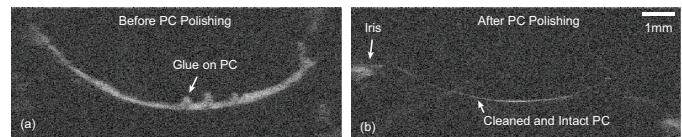

Fig. 19. Representational comparison (a) before and (b) after PC polishing at the same cross-sectional plane.

stabilization by optimized feedback control, and accurate PC polishing trajectory tracking by feedforward filters derived by data-based ILC. In surgical practice, many surgeons skip PC polishing due to the high risk of iatrogenic damage. We have demonstrated automated robotic PC polishing on four *ex-vivo* pig eye with less than 20 μm trajectory tracking error, a reduction of almost 90% over the optimized PID feedback control, and an average of 23 seconds cycle time for complete glue removal with intact PC structure.

the data within the polishing radius was considered, as a result, the OCT resolution and pixel quantization dominate the uncertainties during the manual segmentation procedure. We can then calculate the percentage of glue removal once the glue volume for both of the pre-operative and post-operative volume scans were determined. The calculated percentages of removal were all greater than 98%, meaning the system was able to effectively remove the glue.

The aspiration (p_{asp}) under IOP feedback control was automatically adjusted and recorded intra-operatively during PC polishing (Fig. 18). The gravity feed of the water bottle resulted in more than 40 mmHg in initial IOP. With the IOP regulation, the measured IOP level maintained at the target IOP level over the course of each trail. When the tool started tracking the trajectory, the aspiration force actively adjust to compensate for the IOP change, which demonstrates the success of IOP control.

The polishing procedure starts around 10 s for each trial, which can be seen from the variation in the IOP due to more intraocular volume occupied by the I/A handpiece. However, the aspiration force was able to regulate the IOP pressure to the commanded level. The robot continuously repeated the trajectory until the PC appeared clean from the per-operative OCT B-scans, then the I/A handpiece was withdrawn from the eye at the command of the human operator. By the end of the polishing, the integrity of the PC was assessed by a post-operative volume scan, followed by visual inspection conducted by a trained surgical fellow through the surgical microscope. PCR was not detected in any of the four trials.

VII. CONCLUSION

We have presented innovations in robotic intraocular sugery with enabling mechatronic methods for the effective and efficient robotic PC polishing: docking apparatus for eye stabilization, intraocular pressure regulation for intraocular tissue

REFERENCES

[1] M. Khairallah, R. Kahloun, R. Bourne, H. Limburg, S. R. Flaxman, J. B. Jonas, J. Keeffe, J. Leasher, K. Naidoo, K. Pesudovs *et al.*, "Number of people blind or visually impaired by cataract worldwide and in world regions, 1990 to 2010," *Investigative ophthalmology & visual science*, vol. 56, no. 11, pp. 6762–6769, 2015.
[2] M. Lundström, P.-P. Goh, Y. Henry, M. A. Salowi, P. Barry, S. Manning, P. Rosen, and U. Stenevi, "The changing pattern of cataract surgery indications: a 5-year study of 2 cataract surgery databases," *Ophthalmology*, vol. 122, no. 1, pp. 31–38, 2015.
[3] D. J. Apple, K. D. Solomon, M. R. Tetz, E. I. Assia, E. Y. Holland, U. F. Legler, J. C. Tsai, V. E. Castaneda, J. P. Hoggatt, and A. M. Kostick, "Posterior capsule opacification," *Survey of ophthalmology*, vol. 37, no. 2, pp. 73–116, 1992.
[4] N. Awasthi, S. Guo, and B. Wagner, "Posterior capsular opacification: a problem reduced but not yet eradicated," *Archives of ophthalmology*, vol. 127, no. 4, pp. 555–562, 2009.
[5] D. J. Spalton, "Posterior capsular opacification after cataract surgery," *Eye*, vol. 13, no. 3, pp. 489–492, 1999.
[6] S. Krag and T. T. Andreassen, "Mechanical properties of the human posterior lens capsule," *Investigative ophthalmology & visual science*, vol. 44, no. 2, pp. 691–696, 2003.
[7] J. Gonnermann, S. Al-Mulsi, M. Klamann, A. Maier, M. Pahlitzsch, N. Torun, and E. Bertelmann, "Long-term outcomes and complications after surgical posterior capsule polishing due to secondary cataract," *Klinische Monatsblatter fur Augenheilkunde*, vol. 233, no. 8, pp. 910–913, 2016.
[8] S. Aktan, D. Laws, R. Taylor, and J. Pearce, "Posterior capsule polishing and postoperative opacification in intercapsular cataract surgery," *European Journal of Implant and Refractive Surgery*, vol. 4, no. 3, pp. 161–163, 1992.
[9] J. T. Wilson, M. J. Gerber, S. W. Prince, C.-W. Chen, S. D. Schwartz, J.-P. Hubschman, and T.-C. Tsao, "Intraocular robotic interventional surgical system (iriss): Mechanical design, evaluation, and master–slave manipulation," *The International Journal of Medical Robotics and Computer Assisted Surgery*, vol. 14, no. 1, p. e1842, 2018.
[10] C.-W. Chen, Y.-H. Lee, M. J. Gerber, H. Cheng, Y.-C. Yang, A. Govetto, A. A. Francone, S. Soatto, W. S. Grundfest, J.-P. Hubschman *et al.*, "Intraocular robotic interventional surgical system (iriss): semi-automated oct-guided cataract removal," *The International Journal of Medical Robotics and Computer Assisted Surgery*, vol. 14, no. 6, p. e1949, 2018.

[11] C.-W. Chen, A. A. Francone, M. J. Gerber, Y.-H. Lee, A. Govetto, T.-C. Tsao, and J.-P. Hubschman, "Semiautomated optical coherence tomography-guided robotic surgery for porcine lens removal," *Journal of Cataract & Refractive Surgery*, vol. 45, no. 11, pp. 1665–1669, 2019.

[12] M. J. Gerber, J.-P. Hubschman, and T.-C. Tsao, "Robotic posterior capsule polishing by optical coherence tomography image guidance," *The International Journal of Medical Robotics and Computer Assisted Surgery*, p. eRCS2248, 2021.

[13] B. Wu, G. Williams, A. Tan, and J. Mehta, "A comparison of different operating systems for femtosecond lasers in cataract surgery," *Journal of Ophthalmology*, vol. 2015, 2015.

[14] A. Thorne, D. W. Dyk, D. Fanney, and K. M. Miller, "Phacoemulsifier occlusion break surge volume reduction," *Journal of Cataract & Refractive Surgery*, vol. 44, no. 12, pp. 1491–1496, 2018.

[15] S. A. Bello, S. Malavade, and C. L. Passaglia, "Development of a smart pump for monitoring and controlling intraocular pressure," *Annals of biomedical engineering*, vol. 45, no. 4, pp. 990–1002, 2017.

[16] P.-J. Chen, S. Saati, R. Varma, M. S. Humayun, and Y.-C. Tai, "Wireless intraocular pressure sensing using microfabricated minimally invasive flexible-coiled lc sensor implant," *Journal of Microelectromechanical Systems*, vol. 19, no. 4, pp. 721–734, 2010.

[17] T. Gopesh, A. Camp, M. Unanian, J. Friend, and R. N. Weinreb, "Rapid and accurate pressure sensing device for direct measurement of intraocular pressure," *Translational Vision Science & Technology*, vol. 9, no. 3, pp. 28–28, 2020.

[18] J. Hubschman, J. Son, B. Allen, S. Schwartz, and J. Bourges, "Evaluation of the motion of surgical instruments during intraocular surgery," *Eye*, vol. 25, no. 7, pp. 947–953, 2011.

[19] S. Mariacher, P. Laubichler, M. Mariacher, J. Wendelstein, I. Fischinger, and M. Bolz, "Impact of baseline iop, vacuum, and different docking mechanisms, and their interaction on iop rise in femtosecond laser–assisted refractive and cataract surgery," *Journal of Cataract & Refractive Surgery*, vol. 45, no. 12, pp. 1818–1825, 2019.

[20] J. Liu and C. J. Roberts, "Influence of corneal biomechanical properties on intraocular pressure measurement: quantitative analysis," *Journal of Cataract & Refractive Surgery*, vol. 31, no. 1, pp. 146–155, 2005.

[21] O. Abouali, D. Bayatpour, A. Ghaffariyeh, and G. Ahmadi, "Simulation of flow field during irrigation/aspiration in phacoemulsification using computational fluid dynamics," *Journal of Cataract & Refractive Surgery*, vol. 37, no. 8, pp. 1530–1538, 2011.

[22] A. M. Azhdam, R. A. Goldberg, and S. Ugradar, "In vivo measurement of the human vitreous chamber volume using computed tomography imaging of 100 eyes," *Translational Vision Science & Technology*, vol. 9, no. 1, pp. 2–2, 2020.

[23] S. T. Fontana and R. F. Brubaker, "Volume and depth of the anterior chamber in the normal aging human eye," *Archives of Ophthalmology*, vol. 98, no. 10, pp. 1803–1808, 1980.

[24] C.-W. Chen, S. Rai, and T.-C. Tsao, "Iterative learning of dynamic inverse filters for feedforward tracking control," *IEEE/ASME Transactions on Mechatronics*, vol. 25, no. 1, pp. 349–359, 2019.

Yu-Ting Lai received the B.S. degree in mechanical engineering from National Tsing Hua University, and M.S. degree in electrical engineering from National Chiao Tung University, Hsinchu, Taiwan, in 2016 and 2018, respectively. He is currently working toward the Ph.D. degree in adaptive and iterative learning control with the Mechanical and Aerospace Engineering Department, University of California, Los Angeles, CA, USA.

Matthew J. Gerber received the B.S. and M.S. degrees in Mechanical Engineering from The Ohio State University, Columbus, Ohio in 2013 and 2014, and the Ph.D. degree in Mechanical Engineering from the University of California, Los Angeles in 2019. In 2020, he joined the Stein Eye Institute in the Department of Ophthalmology at the University of California, Los Angeles. His research interests include surgical robotics, computer vision, and mechatronics.

Jaime Dodds received his M.D. degree in 2015 at the Austral Hospital in Pilar, Argentina. He trained as a Internal Medicine resident from 2016 to 2017 at the Buenos Aires British Hospital. From 2017 to 2021 he trained in Ophthalmology at the Dr Charles Ophthalmologic Center in Buenos Aires, Argentina and received his degree from the Salvador University in 2021. He is now an international retina fellow in vitreoretinal diseases in Stein Eye Institute at UCLA.

Jean-Pierre Hubschman trained in Ophthalmology at the Hôpital de la Timone in Marseille, France from 1991 to 1996 and received his M.D. degree from Aix-Marseille University in 1996. He did a fellowship in vitreoretinal surgery from 1996 to 1998 and then headed the Retina department of the Ophthalmologic Center of Saint Jean de Luz (France), the Polyclinique Aguilera Biarritz (France), and the Policlínica Gipuzkoa, San Sebastian (Spain). In 2007, Jean-Pierre Hubschman joined the Retina division of the Stein Eye Institute at UCLA as a Professor of Ophthalmology.

Yu-Hsiu Lee received the B.S. and M.S. degrees in mechanical engineering from National Taiwan University, Taipei, Taiwan, in 2007 and 2009, respectively and the Ph.D. degree in mechanical and aerospace engineering from University of California, Los Angeles (UCLA), Los Angeles, USA in 2019. He is currently an Assistant Professor of Mechanical Engineering at National Taiwan University, Taipei, Taiwan.

Jacob Rosen received the B.Sc. degree in mechanical engineering and the M.Sc. and Ph.D. degrees in biomedical engineering from TelAviv University, Tel-Aviv, Israel, in 1987, 1993, and 1997, respectively. He is currently a Professor with the Department of Mechanical and Aerospace Engineering and the Director of the Bionics Lab, University of California, Los Angeles, Los Angeles, CA, USA. His research interests focus on medical robotics, biorobotics, human-centered robotics, surgical robotics, wearable robotics, rehabilitation robotics, and neural control.

Tsu-Chin Tsao received the B.S. degree in engineering from the National Taiwan University, Taipei, Taiwan, in 1981, and the M.S. and Ph.D. degrees in mechanical engineering from the University of California, Berkeley, in 1984 and 1988, respectively. He is with the University of California, Los Angeles, as Professor in the Mechanical and Aerospace Engineering Department and the Director of Mechatronics and Control Laboratory. His research work and interest include adaptive, repetitive, feedforward, and high-performance control for robotic and mechatronic systems.